Near-field Ultra-wideband mmWave Channel Characterization Using Successive Cancellation Beamspace UCA Algorithm

Zhang, Fengchun; Fan, Wei

Published in:
I E E E Transactions on Vehicular Technology

DOI (link to publication from Publisher):
10.1109/TVT.2019.2926783

Publication date:
2019

Document Version
Accepted author manuscript, peer reviewed version

Near-field Ultra-wideband mmWave Channel Characterization Using Successive Cancellation Beamspace UCA Algorithm

Fengchun Zhang and Wei Fan

***Abstract*—Of the wide palette of 5G features, ultra-wide bandwidth and large-scale antenna configuration are regarded as the essential enabling technology components for millimeter wave (mmWave) communication. Accurate knowledge of delay and angle information of multipath components is essential for many applications in mmWave systems. There is a strong need for a low computation-cost channel estimation algorithm for such systems, where typically adopted far-field and narrowband assumptions might be violated. In this work, a generic yet novel beamspace uniform circular array (UCA) beamforming algorithm with successive cancellation scheme is proposed to jointly detect the impinging azimuth angle and delay of each multipath component. The proposed algorithm is computationally cheap and it works for ultra-wideband (UWB) UCA systems in the near-field conditions as well as the traditional narrowband systems in the far-field conditions. Both numerical simulations and experimental validation results are provided to demonstrate the effectiveness and robustness of the proposed algorithm, compared to the state-of-art works.**

***Index Terms*—Beamspace UCA, phase mode excitation, uniform circular array (UCA), near-field, ultra-wideband, mmWave channel characterization, large-scale antenna systems**

I. Introduction

The next generation wireless communication system, typically referred to as the fifth generation (5G), is currently under intensive research and development. Millimeter wave (mmWave) communication is regarded as one of the enabling components for 5G cellular communication systems, thanks to the large amount of available frequency spectrum [1]–[6]. However, mmWave transmissions suffer from high propagation loss and blockage, unlike sub-6GHz legacy frequency band. High antenna gain (typically realized with a large-scale antenna structure) is required to overcome the radio propagation loss and achieve the good signal-to-noise ratio (SNR) at mmWave bands. Therefore, mmWave transmissions will be potentially ultra-wideband (UWB) (e.g. with an absolute bandwidth larger than 500 MHz) and involve large-scale antenna systems at both communication ends [7], [8]. The far-field assumption holds when the distance between the scattering source and the antenna array is larger than the Fraunhofer distance $2D^2/\lambda$, with D the antenna array aperture and λ the wavelength. The far-field assumption can be violated in short-range mmWave propagation scenarios. It is predicted that a new 5G channel model should be capable of supporting broad bandwidths, e.g., 500 MHz to 4 GHz, and must support massive MIMO, i.e., spherical wavefront must be considered [9]–[12].

It is of importance to understand how the radio signal propagates in the given scenario. A new air interface system design typically starts with the understanding of the deployment scenario, where channel models should be developed to reflect the physical transmission. Accurate knowledge of the delay and angle information of multipath components is essential for many applications in mmWave systems. The extracted multipath components can be further utilized for analysis, clustering and modeling of wireless channels, which is fundamental for system design and performance evaluation [13], [14]. A popular channel sounding setup at mmWave bands is to utilize a nonreal-time channel sounder based on the virtual antenna array concept [15]–[18]. This strategy is simple, flexible and cost-effective, though it is not suitable for dynamic propagation scenarios due to slow mechanical movement of antenna and channel sounding time for each virtual array location. Furthermore, the mutual coupling effects between the array elements are not presented, which is beneficial since it can further simplify the channel estimation. Virtual uniform circular array (UCA) is particularly popular, since it only requiresmechanical movement along circumference and presents approximately constant beam patterns over 360^o azimuth angle, regardless of the steering angle [19], [20].

Channel estimation algorithms proposed in the literature for power-angle-delay profile (PADP) estimation were mainly under the far-field and narrowband assumptions. The narrowband assumption holds when the condition $D/\lambda \ll f/B$ is satisfied, where f is the frequency and B is the bandwidth. When the system bandwidth becomes wide (e.g. in the mmWave context) that the narrowband assumption does not hold anymore for a given array aperture and frequency, the propagation delay of each path can be resolved at different delay bins between array elements. The existing algorithms in the literature would fail to work under near-field and wideband scenarios, as briefly summarized below.

1) Beamforming techniques such as classical beamforming (CBF) and Capon beamforming. As demonstrated in [21], The beam pattern of the CBF method is highly sensitive to near-field conditions (which would introduce a power loss in the target direction) and UWB bandwidth (which would introduce a joint sidelobe in the delay and angle domain and difficult to suppress [21]). Capon beamformer degrades as well in near-field and UWB conditions, since

Fengchun Zhang and Wei Fan are with the APMS section at the Department of Electronic Systems, Faculty of Engineering and Science, Aalborg University, Denmark (email: {fz, wfa}@es.aau.dk. (Corresponding author: Wei Fan)

the steering vectors are typically calculated at the center frequency and under far-field conditions.

2) Subspace methods. The conventional subspace angle estimation methods are based on the element-space covariance matrix, where the steering vector is defined in the center frequency. Thus, it implies the narrowband assumption. UCA is attractive in angle estimation also thanks to its circular symmetry, where beamspace transform of UCA based on the phase mode excitation principle can be applied [22]–[24]. Basically, we can transform the UCA array manifold (in the element space) into Vandermonde structure as uniform linear array (ULA) manifold (in the phase mode space), which enables us to develop computationally efficient and high-resolution subspace algorithms [25]–[29]. However, the aforementioned beam-space multiple signal classification (MUSIC) or estimation of signal parameters by rotational invariance techniques (ESPRIT) algorithms were only investigated under narrowband and far-field assumptions. Subspace methods were also developed for joint angle-delay estimation (JADE). With the JADE strategy, the JADE-MUSIC [30] and the JADE-ESPRIT [31] algorithms exploited both space and time properties by stacking the array element channel impulse responses into a high dimension vector. After performing the eigen-decomposition on the covariance matrix of the constructed vector, JADE can be obtained with either MUSIC or ESPRIT methods. However, both algorithms are unfavorable for the UWB large-scale antenna systems, due to the high complexity introduced by the high dimension of the stacked space-time vector.
3) High resolution parametric methods. Maximum likelihood estimator (MLE) is a popular high resolution channel estimation algorithm. However, the MLE is well-known for its high computational complexity due to its joint estimation mechanism, particularly when the channel parameter dimension is large. An attempt to reduce the MLE computation complexity was proposed in [32], [33]. The space-alternating generalized expectation-maximization (SAGE) algorithm is a relatively low-cost expectation-maximization (EM) algorithm, where the multi-dimensional search is replaced with several one-dimensional searches [34]. However, a prerequisite to utilize the SAGE algorithm is that the likelihood function needs to be independent between different parameter spaces, which might be violated when narrowband and far-field assumptions do not hold, e.g. for the UWB large-scale antenna systems [34]. A general spherical wave model, i.e. including the distance to the scatterer, can be introduced in the MLE type algorithm implementation, which would, however, further increases the computation complexity.

There is a strong need for a low-cost and generic channel estimation algorithm for joint angle and delay profile estimation, which works in practical propagation scenarios, regardless of the antenna system scale (i.e. large or small) and frequency bandwidth settings (i.e. narrow or ultra-wide). That is, it can be applied for the near-field UWB scenarios without increasing the algorithm computation complexity. However, such algorithm is missing in the literature, to the best knowledge of the authors. In this work, a novel low-cost beamspace UCA beamforming algorithm with a successive cancellation scheme is proposed to jointly detect the azimuth angle and delay of the multipath components. The proposed algorithm is insensitive to the system bandwidth and distance to the scatterers, making it suitable for UWB large-scale UCA antenna systems. In this paper, we firstly demonstrate the performance deterioration of CBF of the UCA in the element space when far-field assumption does not hold. To solve the issue, we resort to the beamspace transform of UCA based on the phase mode excitation principle. The beamspace UCA is shown to be robust to phase errors introduced by the spherical wavefront. A novel beamspace UCA algorithm with the successive cancellation of the detected paths is detailed. Both numerical simulations and experimental results at mmWave bands are provided to demonstrate the effectiveness and robustness of the proposed method in channel parameter estimation for UWB large-scale UCA antenna systems. The proposed algorithm was validated by an indoor measurement campaign performed with a virtual UCA channel sounder. The virtual array channel sounder only works for static propagation scenarios, Note that the proposed algorithm should work for dynamic propagation scenarios as well in principle.

II. Problem Statement

Assume a UCA is distributed in the x-y plane and its center is located at the origin of the coordinate system. The UCA consists of P isotropic antenna elements with radius r. The angular position of the p-th element is $\varphi_p = 2\pi \cdot (p-1)/P$, $p \in [1, P]$. Suppose there are N paths impinging at the UCA, the channel frequency response at the p-th UCA element is the superposition of the channel responses of the N paths,

$$H_p(f) = \sum_{n=1}^{N} \alpha_n \exp(-j2\pi f \tau_n) \cdot a_p(f, \mathbf{\Theta}_n), \tag{1}$$

where α_n and τ_n represent the complex amplitude and delay of the n-th path, respectively. $\mathbf{\Theta}_n = [D_n, \theta_n, \phi_n]$ denotes the scatterer location vector of the n-th path, where D_n is the distance between the n-th scatterer and the UCA center, θ_n and ϕ_n the elevation and azimuth angle of the n-th path, respectively. $a_p(f, \mathbf{\Theta}_n)$ is the transfer function between the n-th scatterer and the p-th UCA element, which is normalized by the transfer function between the n-th scatterer and the UCA center, as

$$a_p(f, \mathbf{\Theta}_n) = \beta_{p,n} \exp(-jk\Psi_{p,n}). \tag{2}$$

$\beta_{p,n} = D_n/d_{p,n}$ denotes the relative path loss term at the p-th element with respect to (w.r.t) the UCA center, where $d_{p,n}$ represents the distance between the n-th scatterer and the p-th UCA element. Under far-field assumption, we have $\beta_{p,n} = 1$. $k = 2\pi f/c$ is the wave number with c denoting the speed of light. $\Psi_{p,n}$ indicates the relative propagation distance to the p-th UCA element w.r.t UCA center, i.e.,

$$\Psi_{p,n} = d_{p,n} - D_n, \tag{3}$$

where the distance term $d_{p,n}$ is given by

$$d_{p,n} = \sqrt{D_n^2 + r^2 - 2rD_n \sin\theta_n \cos(\phi_n - \varphi_p)}. \quad (4)$$

Following Taylor series expansion, we can approximate $d_{p,n}$ as

$$d_{p,n} = D_n - r\sin\theta_n \cos(\phi_n - \varphi_p) + \Delta_{p,n}, \quad (5)$$

where $\Delta_{p,n}$ is the term introduced by the near-field condition. When the plane-wave assumption holds, we have $\Delta_{p,n} = 0$. By substituting (5) into (3), $\Psi_{p,n}$ can be simplified as

$$\Psi_{p,n} = -r\sin\theta_n \cos(\phi_n - \varphi_p) + \Delta_{p,n}. \quad (6)$$

In this paper, the objective is to detect path parameters $\{\alpha_n, \tau_n, \phi_n\}$ with elevation angle θ_n ($|\theta_n - 90^o| \leqslant 45^o$) present in the near-field condition for $n \in [1, N]$. The performance of CBF and frequency-invariant beamforming (FIBF) based on UCA for a general 3D multipath scenario under far-field assumption has been discussed in [35]. Below, we limit our discussions on the beamforming properties of CBF and FIBF under near-field conditions, assuming that all impinging paths are confined to the plane of the UCA, i.e. with elevation angle $\theta_n = \frac{\pi}{2}$ for $n \in [1, N]$ for simplicity. Though the proposed algorithm works for 3D propagation scenarios as later discussed in section IV and V.

A. CBF in the UCA element space

Using the CBF under plane-wave assumption, the steering weight of the p-th UCA element can be written as

$$w_p(f, \phi) = \frac{1}{P}\exp[-kr\cos(\phi - \varphi_p)]. \quad (7)$$

Therefore, the UCA array beam pattern can be obtained by taking the coherent summation of the element responses as

$$B(f, \phi) = \frac{1}{P}\sum_{p=1}^{P} w_p(f, \phi) \cdot H_p(f). \quad (8)$$

By taking (1) into (8), we have

$$\begin{aligned} B(f, \phi) &= \sum_{n=1}^{N} \alpha_n \exp(-j2\pi f\tau_n) \cdot \sum_{p=1}^{P} w_p(f, \phi) \cdot a_p(f, \mathbf{\Theta}_n)/P \\ &= \sum_{n=1}^{N} \alpha_n \exp(-j2\pi f\tau_n) \cdot v_n(f, \phi) \\ &= \sum_{n=1}^{N} B_n(f, \phi), \end{aligned} \quad (9)$$

where $B_n(f, \phi)$ represents the beam pattern of the n-th path, i.e. the beam pattern of a single path. As seen from (9), the linear superposition of the CBF beam patterns of all paths gives the beam pattern of the multiple paths. $v_n(f, \phi)$ denotes the unit beam pattern term of the n-th path with CBF. In ideal case, $|v_n(f, \phi)|$ mimics a Dirac delta function in ϕ domain, i.e. $|v_n(f, \phi)| = \delta(\phi - \phi_n)$. Thus the peak location of $|v_n(f, \phi)|$ gives the estimate of ϕ_n. And then α_n and τ_n can be obtained via inverse Fourier transform (IFT) of $B(f, \phi)$ at $\phi = \phi_n$. According to (9), (7) and (2), $v_n(f, \phi)$ can be given by

$$\begin{aligned} v_n(f, \phi) =& \frac{1}{P}\sum_{p=1}^{P} \beta_{p,n} \cdot \exp(-jk\Delta_{p,n}) \\ & \cdot \exp\{-jkr[\cos(\phi - \varphi_p) - \cos(\phi_n - \varphi_p)]\}. \end{aligned} \quad (10)$$

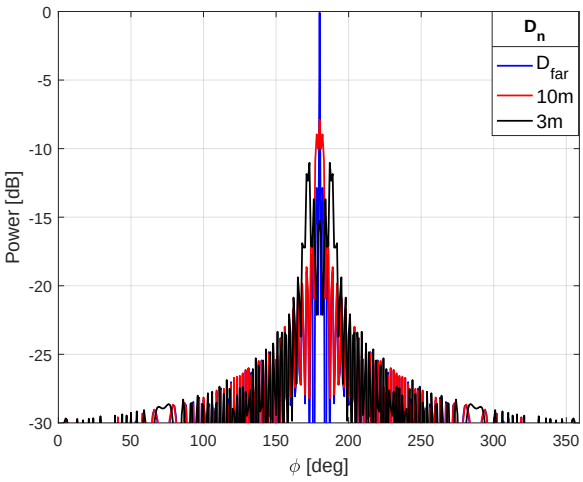

Figure 1. The unit CBF beam pattern $v_n(f, \phi)$ in the UCA element space for different D_n with $\theta_n = \pi/2$, $\phi_n = \pi$, r = 0.5 m, f = 29 GHz and $P = 720$ are set for the UCA. The calculated Fraunhofer far-field distance $D_{far} = 2(2r)^2/\lambda$ is around 193 m.

Under the far-field condition (i.e. $\beta_{p,n} = 1$ and $\Delta_{p,n} = 0$), we have $|v_n(f, \phi_n)| = 1$ and $|v_n(f, \phi_{n'})| < 1$ with $\phi_{n'} \neq \phi_n$, as illustrated by the blue line in Fig.1. Thus the peak location in the beam pattern gives the angle estimate of the n-th path.

To investigate whether $|v_n(f, \phi)|$ can still maintain this property under near-field condition, we reduce the distance D_n and its effect on the beam patterns of $v_n(f, \phi)$ is shown in Fig. 1. The results show that the beam patterns are highly susceptible to phase errors introduced by the spherical wavefront in the near-field condition. The near-field condition results in the main beam distortion of the beam pattern, including the power loss (the red curve) and the concave pattern in the target direction (the black curve). The power loss results in underestimating the amplitude α_n and the concave pattern would result in fake path angle detection.

To further investigate the power loss in the target direction under near-field condition, the distance from 3 m to 70 m is set and the result is shown by the blue dotted line in Fig. 2. The figure shows that with CBF method, a power loss more than 35 dB might exist in the target direction for typical indoor scenarios.

Therefore, besides the joint sidelobe problem introduced by the UWB bandwidth in PADP as shown in [21], the CBF of UCA in the element space would also suffer from significant power loss in target directions or even failure of detecting the true paths, due to phase errors introduced in the near-field condition, which makes it unsuitable for channel parameter estimation of mmWave UWB large-scale antenna systems.

B. Beamformer in the UCA phase mode space

The frequency response of the UCA element space can be converted to phase mode space as

$$\underline{H}_m(f) = \frac{1}{P}\sum_{p=1}^{P}\hat{G}_m(f)\cdot\exp(jm\varphi_p)\cdot H_p(f), \tag{11}$$

where $\underline{H}_m(f)$ denotes the m-th mode response of the UCA in the phase mode space and $\hat{G}_m(f)$ represents the compensation filter.

By taking equation (1) into (11) and changing the order of the two summations, we have

$$\begin{aligned}\underline{H}_m(f) =& \sum_{n=1}^{N}\alpha_n\exp(-j2\pi f\tau_n)\\ &\cdot\left\{\frac{1}{P}\sum_{p=1}^{P}\hat{G}_m(f)\exp(jm\varphi_p)\cdot a_p(f,\boldsymbol{\Theta}_n)\right\}\\ =&\sum_{n=1}^{N}\alpha_n\exp(-j2\pi f\tau_n)\cdot\underline{a}_m(f,\boldsymbol{\Theta}_n),\end{aligned} \tag{12}$$

where $\underline{a}_m(f,\boldsymbol{\Theta}_n)$ is given by the $\{\cdot\}$ term in the above equation. Comparing the above equation with (1), we can see that for the n-th path, $\underline{a}_m(f,\boldsymbol{\Theta}_n)$ is the UCA manifold of the m-th mode in the phase mode space and $a_p(f,\boldsymbol{\Theta}_n)$ defined in (2) is the UCA manifold of the p-th element in the element space.

As discussed in [35], $\underline{a}_m(f)$ can be approximated to $\underline{a}_m(f) = \exp(jm\phi_n)$ under far-field condition and with all paths confined in the UCA plane, i.e. $\theta_n = 90^o, n \in [1, N]$, where the compensation filter was defined as $\hat{G}_m(f) = 1/[j^m J_m(kr)]$ with $J_m(\cdot)$ denoting the Bessel function of the first kind with order m. However, in practical propagation scenario, it is very unlikely that the incident paths are strictly limited to the UCA plane. Therefore, we modified the compensation filter for 3D propagation scenarios as [35],

$$\frac{1}{\hat{G}_m(f)} = 0.5j^m[J_m(kr) - jJ_m^{'}(kr)], \tag{13}$$

where $(\cdot)^{'}$ denotes the differential operator.

The beam pattern of the FIBF can be written as

$$\underline{B}(f,\phi) = \frac{1}{2M+1}\sum_{m=-M}^{M}\exp(-jm\phi)\cdot\underline{H}_m(f), \tag{14}$$

where $\exp(-jm\phi)/(2M+1)$ is the steering weight of the m-th phase mode. Substituting the array phase mode response $\underline{H}_m(f)$ defined in (12) into the above equation and rearranging the summation order, we have

$$\begin{aligned}\underline{B}(f,\phi) =& \sum_{n=1}^{N}\alpha_n\exp(-j2\pi f\tau_n)\cdot\underline{v}_n(f,\phi)\\ =&\sum_{n=1}^{N}\underline{B}_n(f,\phi),\end{aligned} \tag{15}$$

where $\underline{B}_n(f,\phi)$ represents the FIBF beam pattern of the n-th path, i.e. the FIBF beam pattern of a single path. The FIBF beam pattern of the multiple paths is obtained by the linear superposition of the FIBF beam patterns of all paths. Similar to the unit beam pattern term $v_n(f,\phi)$ of CBF, $\underline{v}_n(f,\phi)$ indicates the unit FIBF beam pattern term of the n-th path, which is expressed by

$$\underline{v}(f,\phi) = \frac{1}{2M+1}\sum_{m=-M}^{M}\underline{a}_m(f,\boldsymbol{\Theta}_n)\exp(-jm\phi), \tag{16}$$

where $\underline{a}_m(f,\boldsymbol{\Theta}_n)$ is given in (12).

Similar to the discussions about the unit beam pattern term $v_n(f,\phi)$ of CBF in section II-A, we study the property of $|\underline{v}_n(f,\phi)|$ for various distance D_n. With the same simulation setting as for CBF in Fig. 1, we can plot the unit FIBF beam pattern $\underline{v}_n(f,\phi)$ in Fig. 3. The results show that the beam pattern is insensitive to phase error introduced by the spherical wavefront in the near-field conditions, where an approximately constant beam pattern is achieved for different distance D_n within a large dynamic range.

We further investigate the power loss in the target direction under near-field conditoins for FIBF and the results are shown by the red dotted curve in Fig. 2. It shows that the power values of the target direction are approximately unchanged with different distances D_n.

The unit FIBF beam pattern peaks in the target direction and the peak value keeps approximately constant (approximates to 1) for various distances setting, as shown in Fig. 2. It indicates that the path can be accurately detected with FIBF method under both near-field and far-field conditions.

As detailed in [35], the FIBF method with modified compensation filter works in 3D scenarios, when the elevation angles are not confined to the UCA plane. The above simulation results indicate that the proposed FIBF method can also be applied in near-field scenarios, since the beamformer pattern is insensitive to the introduced phase errors. Thus, the proposed FIBF method can be applied in 3D near-field scenarios. As discussed in [35], the joint PADP can be directly obtained with the modified FIBF, which is simple, effective and robust. However, the resulting PADP suffers from high sidelobes, as shown in Fig. 3. In the next section, a FIBF algorithm with the successive cancellation of the detected paths is detailed, with the objective to eliminate the high sidelobes of the dominant paths.

III. Proposed beamspace UCA with the successive cancellation scheme for near-field scenarios

As discussed, the beamspace UCA with the modified compensation filter $\hat{G}_m(f)$ can achieve constant beam patterns, insensitive to the distances between the scatterers and the UCA center, which makes it suitable for angle estimation in near-field scenarios. In this section, a novel FIBF based on successive cancellation principle to estimate azimuth angle, delay and power of each multipath component is proposed for near-field scenarios, where the paths are detected one by one with the power values in a descending order.

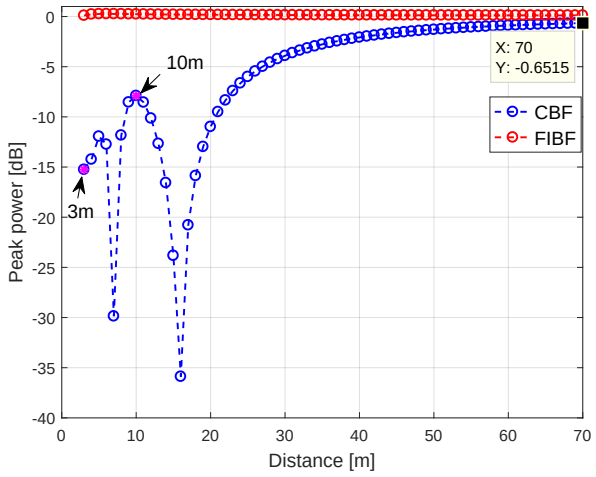

Figure 2. The main beam peak varies with D_n for CBF and FIBF, where $\theta_n = \pi/2$ and $\phi_n = \pi$,f = 29 GHz and $P = 720$ are set for the UCA.

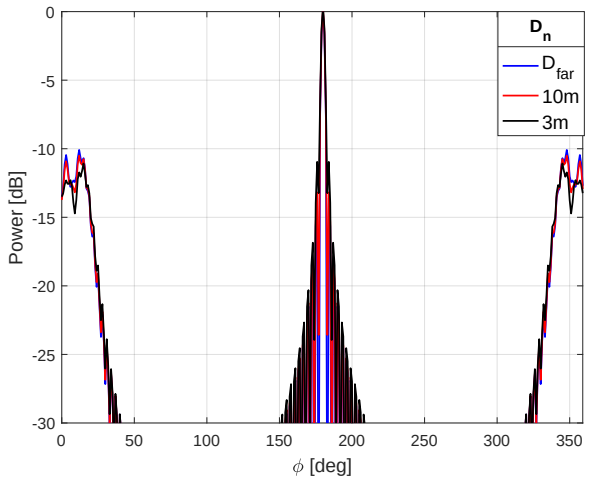

Figure 3. The unit FIBF beam pattern $\underline{v}_n(f,\phi)$ in the UCA phase mode space for variant D_n with $\theta_n = \pi/2$, $\phi_n = \pi$, r = 0.5 m, f = 29 GHz and $P = 720$. The calculated Fraunhofer far-field distance $D_{far} = 2(2r)^2/\lambda$ is around 193 m.

As mentioned in paper [35], the PADP with modified FIBF can be directly obtained by performing IFT of $\underline{B}(f,\phi)$ in (15) as,

$$\begin{aligned}\underline{b}(\tau,\phi) &= \sum_{f=f_1}^{f_L} \underline{B}(f,\phi)\exp(j2\pi f\tau) \\ &= \sum_{n=1}^{N}\sum_{f=f_1}^{f_L} \underline{v}_n(f,\phi)\cdot\alpha_n \exp[j2\pi f(\tau-\tau_n)] \\ &= \sum_{n=1}^{N} \underline{b}_n(\tau,\phi),\end{aligned} \tag{17}$$

where $\underline{b}_n(\tau,\phi)$ is the PADP of the n-th path.

In the ideal case, the PADP mimics the Dirac delta function which peaks at the unique angle-delay positions, i.e. (ϕ_n,τ_n) with desired power values. However, as discussed, $\underline{v}_n(f,\phi)$ presents strong sidelobes at azimuth angle around $\phi_n \pm \pi$ for $n \in [1,N]$. Therefore, weak desired paths might be buried by undesired sidelobes of strong paths. Below, a novel algorithm following the successive cancellation principle is proposed to tackle this problem.

A. Algorithm description

The array element response vector $\mathbf{H}(f)$ is defined as

$$\mathbf{H}(f) = [H_1(f);...;H_P(f)], \tag{18}$$

where $H_p(f)$ was defined in (1).

In the following algorithm description, we add the superscript numbers to the array element response vector $\mathbf{H}(f)$ and PADP $\underline{b}(\tau,\phi)$ to indicate that these terms need to update for each iteration. The superscript number q denotes that q path(s) are removed. For example, $\mathbf{H}^1(f)$ denotes the array element response vector with 1 path removed and $\underline{b}^2(\tau,\phi)$ represents the PADP with 2 paths removed. Typically, the initial array element response vector and PADP are represented with superscript number $q = 0$, i.e. $\mathbf{H}^0(f)$ and $\underline{b}^0(\tau,\phi)$, respectively.

The procedure is detailed as below:

1. Based on the current array element response vector $\mathbf{H}^0(f)$, we apply equations (11), (13), (14) and (17) to obtian the current PADP $\underline{b}^0(\tau,\phi)$.
2. We find the peak location in the current PADP $\underline{b}^0(\tau,\phi)$, which gives the delay and azimuth angle estimation of path 1, i.e. $\hat{\tau}_1$ and $\hat{\phi}_1$, respectively. By taking the estimated delay and azimuth angle back to the original PADP $\underline{b}(\tau,\phi)$, we can obtain the amplitude estimation of path 1, i.e. $\hat{\alpha}_1 = |\underline{b}(\hat{\tau}_1,\hat{\phi}_1)|$.
3. We remove path 1 from the array element response vector $\mathbf{H}^0(f)$ to obtain the updated array element response $\mathbf{H}^1(f)$ as detailed below.

   3.1. The frequency response vector of the UCA elements corresponding to path 1, can be synthesized based on the detected path parameters with $\hat{\theta}_1 = 90^o$ under plane-wave assumption as:

   $$\hat{\mathbf{H}}(f) = \hat{\mathbf{a}}(f,\hat{\phi}_1)\cdot\hat{\alpha}_1\exp(-j2\pi f\hat{\tau}_1), \tag{19}$$

   where $\{\hat{\alpha}_1,\hat{\phi}_1,\hat{\tau}_1\}$ are parameters estimated in step 2 and $\hat{\mathbf{a}}(f,\hat{\phi}_1) \in \mathbb{C}^{P\times 1}$ is the array manifold under plane-wave condition for path 1. The p-th entry of $\hat{\mathbf{a}}(f,\hat{\phi}_1)$ is given by

   $$\hat{a}_p(f,\hat{\phi}_1) = \exp[jkr\cos(\hat{\phi}_1 - \varphi_p)]. \tag{20}$$

   3.2. The synthetic channel impulse response (CIR) vector $\hat{\mathbf{h}}(\tau)$ corresponding to path 1 over array elements and the current CIR vector $\mathbf{h}^0(\tau)$ can be directly obtained via performing IFT of $\hat{\mathbf{H}}(f)$ and $\mathbf{H}^0(f)$, respectively.

   3.3. Generate a label vector $\mathbf{s}(\tau)$ with the same size as $\hat{\mathbf{h}}(\tau)$, where the p-th entry is obtained as

   $$s_p(\tau) = \begin{cases} 0, & |\hat{h}_p(\tau)| > \hat{\alpha}_1\cdot 10^{\frac{-\eta_t}{20}} \\ 1, & otherwise \end{cases} \tag{21}$$

where η_t denotes the threshold value in decibels and $\hat{h}_p(\tau)$ the p-th entry of synthetic CIR vector $\hat{\mathbf{h}}(\tau)$. The entries of $\hat{\mathbf{h}}(\tau)$ with dominant power values are labelled to 0 in the label vector $\mathbf{s}(\tau)$.

The objective of the label vector $\mathbf{s}(\tau)$ is to mark the trajectory of the estimated path in the CIRs over array elements. As explained in step 3.1 and 3.2, we can reconstruct the path trajectory over array elements by using the estimated delay, azimuth angle and amplitude of the path under plane-wave assumption. The label vector would enable us to remove the estimated path from the CIR over array elements in Step 3.4.

3.4. Remove path 1 from the current CIR vector $\mathbf{h}^0(\tau)$ to obtain the updated CIR vector $\mathbf{h}^1(\tau)$ by

$$\mathbf{h}^1(\tau) = \mathbf{h}^0(\tau) \odot \mathbf{s}(\tau), \tag{22}$$

where $\odot$ denotes element-wise multiplication.

3.5. By performing Fourier transform (FT) on the updated CIR vector $\mathbf{h}^1(\tau)$, we can obtain the updated array element response vector $\mathbf{H}^1(f)$.

4. Repeat the above steps until the estimated power of the path is not within the preset dynamic range.

Note that the superscript numbers of the array element response vector and PADP increase 1 for each iteration. For instance, in the n-th iteration, the current array element response vector and PADP are $\mathbf{H}^{n-1}(f)$ and $\underline{b}^{n-1}(\tau,\phi)$, respectively. After step 3.5, we obtain the path parameters $\{\hat{\alpha}_n, \hat{\phi}_n, \hat{\tau}_n\}$ and the array element response vector is updated to $\mathbf{H}^n(f)$.

It is also noted that in step 2, the amplitude estimation of the path is based on the original PADP $\underline{b}(\tau,\phi)$ without superscript, which is kept unchanged for all iterations. Therefore, the amplitude estimations of all the paths are obtained based on the origianl PADP instead of the updated PADP. The reason is that, when the paths, e.g. path n_1 and n_2 with $n_1 < n_2$, have similar or same delays, the trajectories of the two paths are overlapped. As a result, the trajectory of path n_2 will be partly removed as we intend to remove path n_1 in step 3.4. Thus the amplitude estimation of path n_2 based on the updated PADP will be underestimated. This will be further illustrated in the simulation section.

The whole procedure of the proposed path estimation algorithm is summarized in Algorithm 1. Note that η is the preset dynamic range in decibel.

Algorithm 1: The proposed algorithm

Input : $\mathbf{H}(f)$
Output: $\{\hat{\alpha}_n, \hat{\phi}_n, \hat{\tau}_n\}, n \in [1, N]$

```
n := 1;
α̂_{n-1} := 1 , α̂_max := 1 ;
H^{n-1}(f) := H(f), h^{n-1}(τ) := IFT(H(f));
while α̂_{n-1} > (α̂_max · 10^{-η/20}) do
    Perform phase mode space beamforming based on H^{n-1}(f) and obtain the PADP b̲^{n-1}(τ,φ). // Eqs. (11), (13), (14) and (17);
    Detect the strongest path of PADP b̲^{n-1}(τ,φ) and obtain the path parameters {α̂_n, φ̂_n, τ̂_n};
    Remove the detected path from CIR vector h^{n-1}(τ) and update the CIR vector to h^n(τ) ;
    α̂_max := α̂_1, n := n + 1.
end while
```

B. Discussion

The basic principle of the low-cost successive cancellation scheme is that the propagation delay value among UCA array elements are insensitive to D_n (i.e. distance between the array center and the n-th scatterer location) and elevation angles. Therefore, we can remove the detected path based on the azimuth and delay values under the plane-wave assumption and with elevation angle set to 90^o. To investigate the effectiveness of the idea, a single path scenario is considered here. We can utilize the residual power rate R_p to evaluate how effective the detected path is removed from the CIR, which is defined as

$$R_p = \frac{\left\| vec\{\mathbf{h}^1(\tau)\} \right\|^2}{\left\| vec\{\mathbf{h}(\tau)\} \right\|^2} \times 100\%, \tag{23}$$

where $vec\{\cdot\}$ represents vectorization of a matrix and $\|\cdot\|$ indicates the Euclidean norm of the vector.

The high residual power rate means that the deviation between the trajectory of the synthetic CIR vector $\hat{\mathbf{h}}(\tau)$ and the true CIR vector $\mathbf{h}(\tau)$ is large, and the trajectory of the detected path will not be properly removed in the updated CIR vector $\mathbf{h}^1(\tau)$. The consequence is that we will estimate the residual trajectory as the fake path if the residual power is within the preset dynamic range.

Below, we simulate a single path case to illustrate the residual power rate R_p w.r.t bandwidth, distance D and the elevation angle θ_o. In the simulation, a single path with a fixed incident azimuth angle $\phi_0 = 180^o$ impinging at a UCA of radius $r = 0.5$ m is set. The UCA consists of 720 elements with half-wavelength spacing. Besides, we set the center frequency to 29 GHz, the bandwidth from 400 MHz to 3 GHz, distance D from 3 m to 30 m and elevation angle from 90^o to 120^o.

The impact of system bandwidth, distance D and elevation angle θ_o on the residual power rate is shown in Fig. 4.

- For a given bandwidth and elevation angle θ_o, R_p decreases as D increases due to the fact that the larger the D is, the closer we approximate the plane-wave condition, resulting in a smaller R_p.
- For a given distance D and elevation angle θ_o, R_p increases as bandwidth broadens. The wider the bandwidth, the higher the delay resolution we have. As a result, the larger reconstructed CIR error will be detected as the bandwidth becomes wider, which leads to a larger R_p.
- For a given bandwidth and distance D, R_p increases when elevation angle θ_o gets further away from the UCA plane, i.e. with $\Delta\theta = |\theta_o - 90^o|$ becoming larger. This is due to the fact that the synthetic CIR was calculated with $\hat{\theta}_o = 90^o$ in (19) and (20). The larger the elevation angle

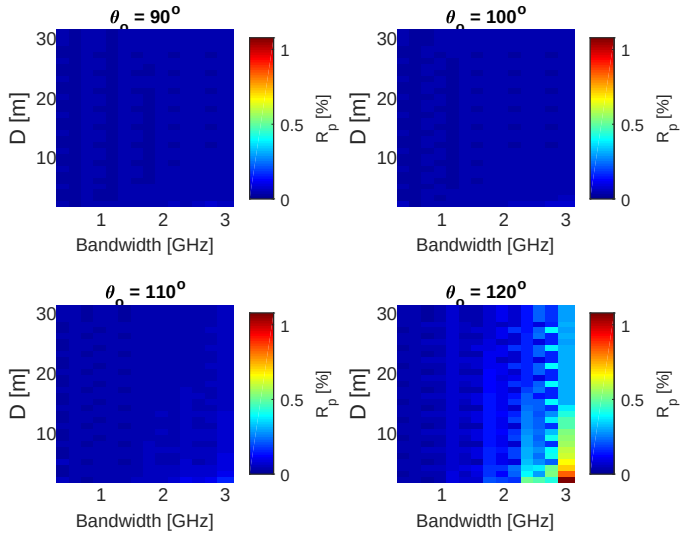

Figure 4. The residual power rate R_p varies with bandwidth, distance D and elevation angle θ_o, where $f_c = 29$ GHz, $\phi_o = \pi$ and $\tau_o = 0$ ns.

away from the UCA plane is, the larger error will be introduced to the reconstructed CIR. The maximum R_p are 0.06%, 0.07%, 0.16% and 1.1% when elevation angle θ_o are set to 90^o, 100^o, 110^o and 120^o, respectively.

For a practical measurement setting with bandwidth less than 3 GHz, the scatterer distance larger than 3 m and the elevation angle $|\theta_o - 90^o| \leqslant 30^o$, the residual power rate is up to 1.1%, as shown in Fig. 4. Therefore, the proposed algorithm works well for practical measurement settings. The proposed cancellation scheme is low-cost, since it only requires the estimated delay and azimuth angle values to remove the detected path. It is effective and robust, as demonstrated in the numerical simulations.

As a summary, the basic principle of the low-cost successive cancellation scheme is that the propagation delays among the UCA elements are insensitive to the elevation angle (for a given elevation angle range) of the path and the distance between the UCA center and the scatterer location. Therefore, we can effectively remove the detected path based on azimuth angle and delay of the path in the updated delay profile among elements. Due to the sparsity of mmWave channels, typically only a few iterations are needed to extract all multipath components. As shown, for each iteration, we obtain the delay and azimuth angle estimate based on the power spectra, which essentially is calculated from the one-dimensional beamforming operation in (14) and IFT operation in (17). Therefore, the computational cost is significantly lower, compared to typical high resolution algorithms, where expensive joint search in multiple parameter domains is required.

IV. Simulation Results

In the simulation, we consider a UCA composed of 720 isotropic antennas with radius 0.5 m and half-wavelength element spacing. The frequency band is from 28 - 30 GHz with 750 frequency points.

A. Algorithm performance evaluation

We simulate a representative yet critical scenario for the channel estimation algorithm, where path 1 and path 3 have the same impinging azimuth angle ϕ at 90^o. Path 2 has an incident angle of 270^o, yet it has the same delay as path 3. In addition, the elevation angles are not strictly confined to the UCA plane as detailed in Table I. The critical scenario is intentionally set to demonstrate the robustness of the algorithm.

Three beamforming algorithms, i.e. CBF [21], FIBF [35] and the proposed algorithm, are compared in Fig. 5. As shown in Fig. 5 (top), though target paths can be roughly detected in the PADP, the CBF algorithm under far-field assumption presents two major drawbacks as explained in Section II-A, i.e. susceptible to strong joint side lobes and main lobe distortions. The PADP with the FIBF algorithm is shown in Fig. 5 (middle). The FIBF suffers from strong side lobes around azimuth angle $\phi_n \pm \pi$ for $n \in [1, N]$ with a shifted delay. The estimated parameters $\{\hat{\alpha}_n, \hat{\phi}_n, \hat{\tau}_n\}, n \in [1, N]$ with the proposed algorithm are shown in Fig. 5 (bottom). The estimated parameters agree well with the targets, with a deviation in path power within 0.3 dB. The small power deviation is caused by the power variance over the UCA elements in the near-field scenario. Based on the Friis free space propagation equation, the maximal power deviation over the UCA elements for a single path case can be evaluated by the ratio of the maximal and minimal power across the UCA elements, i.e., $\rho = \frac{D+r}{D-r}$, where r denotes the radius of the UCA and D the distance between the scatterer and the UCA center with $D > r$. In the far-field case (i.e. $D \gg r$), we have $\rho \approx 1$. However, the power over the UCA elements varies in the near-field case.

Below, we detail the procedure how the path parameters are estimated with the proposed algorithm. To detect the most dominant path, we can follow the procedure below:

1. We can perform the phase mode beamforming based on $\mathbf{h}^0(\tau)$ (i.e. the raw CIR vector $\mathbf{h}(\tau)$), as shown in Fig. 6 (top), and the obtained PADP $\underline{b}^0(\tau, \phi)$ is shown in Fig. 7 (top).
2. From the PADP, we can detect the strongest path, i.e. path 1 as shown in Fig. 7 (top) with path parameters $\hat{\alpha}_1 = 0.2$ dB, $\hat{\phi}_1 = 90^o$ and $\hat{\tau}_1 = 16.6$ ns.
3. Then, we remove path 1 from the initial CIR vector $\mathbf{h}^0(\tau)$ and obtain the updated CIR vector $\mathbf{h}^1(\tau)$ as shown in Fig. 6 (upper-middle).
4. In the end, $\hat{\alpha}_{max} = \hat{\alpha}_1$ is set.

We can repeat the above procedure to detect the second and third paths. The detected path parameters of path 2 and path 3 are $\{\hat{\alpha}_2 = -2.8$ dB, $\hat{\phi}_2 = 270^o, \hat{\tau}_2 = 40.1$ ns $\}$ and $\{\hat{\alpha}_3 = -18.1$ dB, $\hat{\phi}_3 = 90^o, \hat{\tau}_3 = 40.1$ ns $\}$, respectively. In the end, a path with power value within 40 dB dynamic range can not be found based on $\mathbf{h}^3(\tau)$ and therefore the channel estimation procedure is complete.

We can clearly see that the detected path is removed in the updated CIR, e.g. path 1 is removed in the updated CIR vector $\mathbf{h}^1(\tau)$ as shown in 6 (upper-middle). Thus the influnce of the path is also eliminated in the updated PADP $\underline{b}^1(\tau, \phi)$ as shown in 7 (upper-middle). In this simulation, path 2 and 3 have the

Table I
PATH PARAMETERS

Path	1	2	3
α [dB]	0	-3	-18
ϕ [deg]	90	270	90
θ [deg]	90	95	100
D [m]	4.98	12	12
τ [ns]	16.6	40.0	40.0

same delays and therefore the trajectories of the two paths are overlapped, as shown in Fig. 6 (upper-middle). When we remove path 2, the trajectory of path 3 will be partly removed, as illustrated in Fig. 6 (lower-middle). As discussed in section III, to avoid underestimating the amplitude of path 3 $\hat{\alpha}_3$, we estimate the amplitude based on the original PADP $\underline{b}(\tau, \phi)$ as shown in Fig. 5 (middle).

B. Impact of elevation angle

As detailed in [35], the beamformer in the UCA phase mode space with the modified compensation filter works in 3D propagation scenarios when the elevation angle is not restricted to the UCA plane. The beam patterns are approximately constant with different elevation angles. When the elevation angle gets away from the UCA plane, i.e. with $\Delta\theta_n = |\theta_n - 90^o|$ getting larger, the main beam peak drops slightly and the sidelobes of the beamforming pattern at $\phi = \phi_n \pm \pi$ becomes broader.

In order to thoroughly investigate the impact of elevation angle on path parameter detections (i.e. delay, azimuth angle and power), we sweep the elevation angle of the second path from 90^o to 145^o with a 5^o step, while other path parameters are kept unchanged as specified in Table I.

The path parameter estimation results with various θ_2 are shown in Fig. 8. As we can see, the larger the elevation angle is, the larger error will be introduced. When we have elevation angle $|\theta_2 - 90^o| \leq 45^o$, the impact of elevation angle on the path parameter detection is negligible:

1) The azimuth angle and delay detection accuracy of path 1 and 3 is not affected by the elevation angle of the second path. The amplitude detection accuracy of the second path is only slightly affected as the elevation angle increases, i.e., up to 2.5 dB deviation is introduced for elevation angle 135^o.
2) No artefact path is created within the 35 dB dynamic range. As shown in the figure, the amplitude of the artefact path will increase as the elevation angle increases. However, it is still negligible for elevation angle 135^o, with the path amplitude less than -43 dB.

When the elevation angle is far away from the azimuth plane, i.e. $|\theta_2 - 90^o| > 45^o$. There is some impact of the elevation angle on the path parameter detection:

1) The amplitude estimate of the second path is underestimated.
2) The artefact path becomes visible due to the fact that the residual power ratio is large when $|\theta_2 - 90^o| > 45^o$.

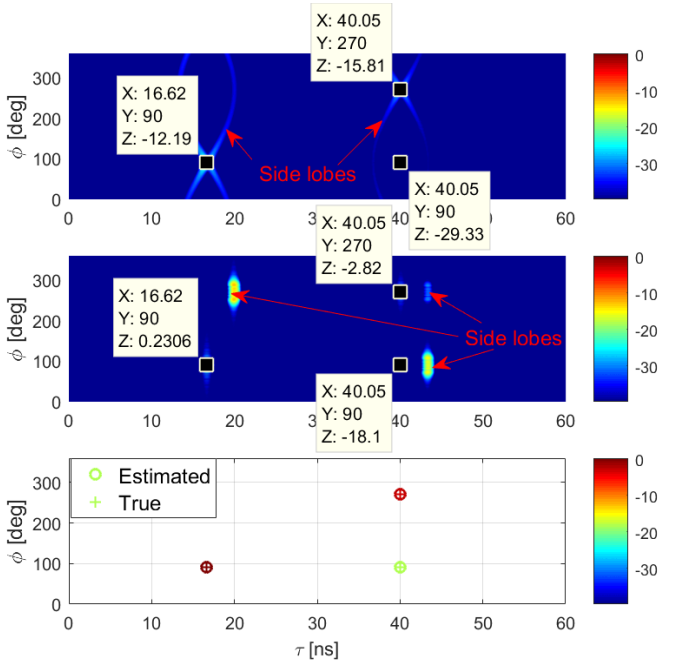

Figure 5. The PADPs with CBF (top), FIBF (middle) and the proposed successive FIBF (bottom).

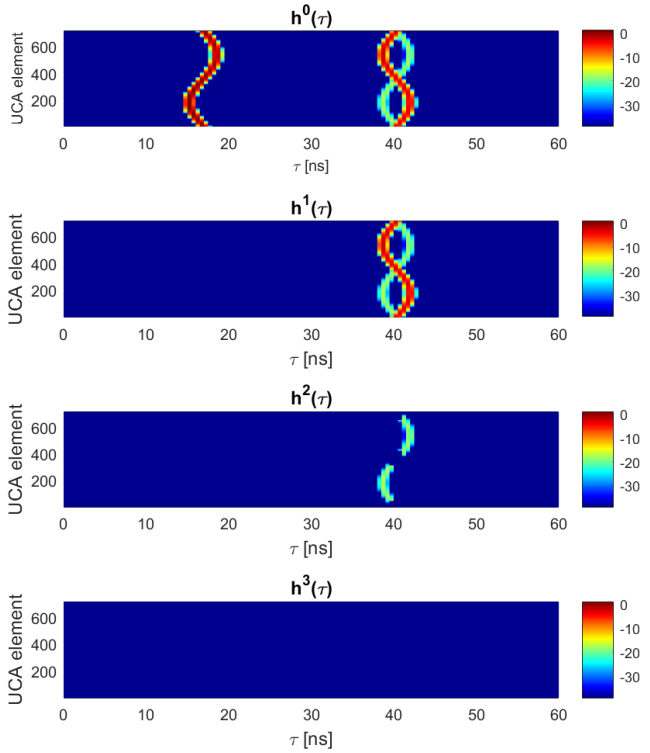

Figure 6. The CIR vectors of $\mathbf{h}^{n-1}(\tau), n \in [1, 4]$, where the superscript denotes the $(n-1)$ path(s) are removed.

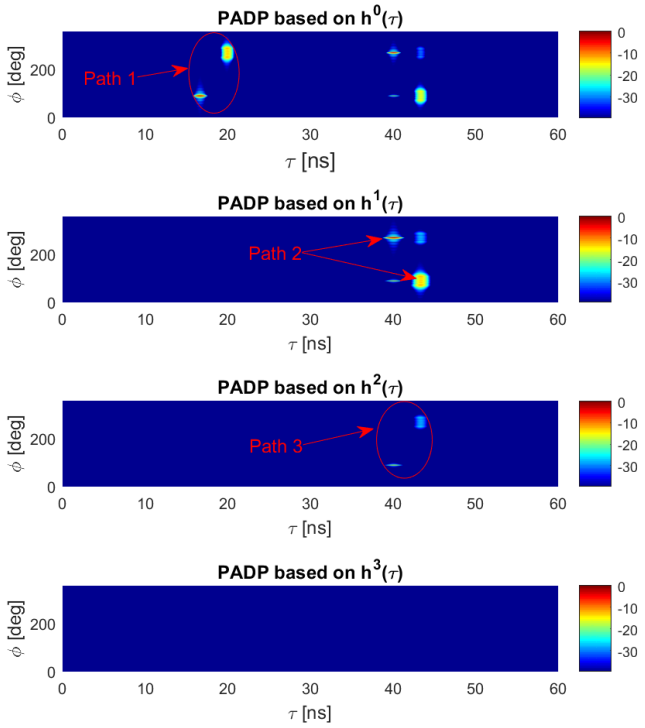

Figure 7. The PADPs based on $\mathbf{h}^{n-1}(\tau), n \in [1, 4]$, where the superscript denotes the $(n-1)$ path(s) are removed.

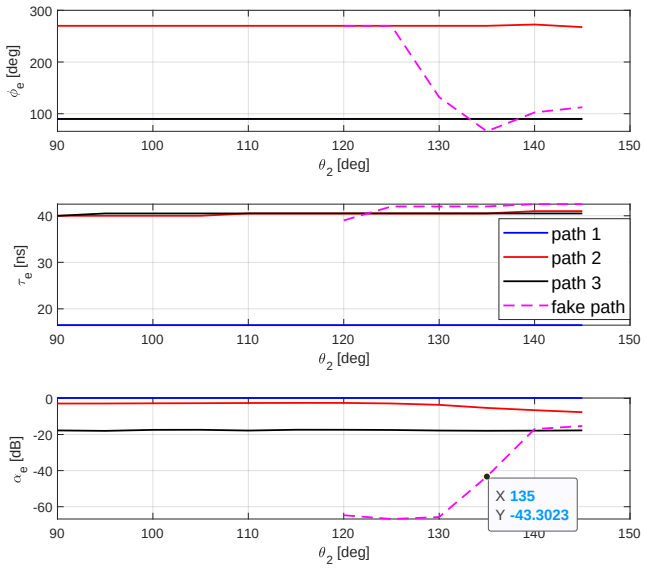

Figure 8. Path parameter estimation results with various θ_2.

V. Measurement Results

A. Introduction

To verify how well the proposed algorithm works in practice, we validate it with practical measurements. The detailed description of the measurement campaign was given in [21] and only outlined here. The measurements were conducted in a typical indoor basement with the floor dimensions of 7.7 m $\times$ 7.9 m. The basement was empty with few objects including a metallic heater and a metallic ladder leaned against the wall. Both line-of-sight (LOS) and obstructed LOS (OLOS) scenarios were considered. The OLOS scenario was created by placing a 1.2 m $\times$ 1.2 m metallic blackboard to block paths in LOS directions.

A wideband biconical antenna with a gain of 6 dB at 28-30 GHz was used at the transmit (Tx) side. The Tx antenna was mounted 0.84 m above the floor. While an identical biconical antenna was exploited at the receive (Rx) side. The Rx antenna was mounted on a turntable with the same height as the Tx antenna. The distance between the Rx antenna and the rotation center was adjusted to 0.5 m. Then a virtual UCA of radius $r = 0.5$ m at Rx side were obtained by rotating the Rx antenna on the turntable. The frequency response of the p-th UCA element was measured when the Rx antenna was rotated to the angular position $\varphi_p = 2\pi \cdot (p-1)/P, p \in [1, P]$ with $P = 720$. For each virtual UCA element, the frequency response was measured with a vector network analyzer (VNA) from 28-30 GHz with 750 frequency points.

The rotational horn antenna measurement was used as a reference. In the rotational horn antenna measurement, the biconical antenna at the Rx side was replaced by a horn antenna with a gain of 19 dB at 28-30 GHz. The horn antenna was positioned at the rotation center of the turntable (i.e. $r = 0$ m) with the same height as the Tx antenna (i.e. 0.84 m above the floor). The same measurement settings (the same Tx antenna, the same frequency sweep and orientation sweep) adopted in biconical antenna UCA measurements were used in rotational horn antenna measurements for comparison purpose.

Note that mutual coupling effect is not present with the virtual array measurement, which is desirable for the channel characterization purpose. The distance between the Tx and the center of the Rx array is around 5 m, while the far-field distance at 30 GHz for the UCA is around 200 m. The system bandwidth in the measurement is larger than 500 MHz and the UCA array aperture (i.e. 1m) is much larger than the delay resolution multiplied by the speed of light (i.e. 0.15 m). Therefore, for the measurement data, both the far-field assumption and narrowband assumption are violated. Note that the antenna gains of both Tx and Rx antennas are de-embedded in measured CIRs. Further, to focus on the specular and dominant multipath components detection, a dynamic range of 30 dB is set in the measurement section.

B. Measured results

The measured CIRs over virtual UCA elements (i.e. measured locations) for the LOS scenario are shown in Fig. 9 (top), where a few specular paths can be clearly detected besides the dominant LOS path. The mmWave channels are more sparse

compared to sub-6GHz channels. In our measurements, the measurement was performed in an empty indoor basement, with no furniture, which also results in sparse channel profiles. The synthetic CIRs over UCA elements for the LOS scenario are shown in Fig. 9 (below). The synthetic CIRs over virtual UCA elements are reconstructed based on detected multipath component parameters $\{\hat{\alpha}_n, \hat{\phi}_n, \hat{\tau}_n\}$ for $n \in [1, N]$ under the plane-wave assumption. The synthetic results agree well with the measured data, indicating a consistent estimation result. The trajectories of the paths over UCA elements match well with the measured ones, even for weak multipath components. The measured PADP with rotational horn antenna is shown in Fig. 10 (top). As shown in the measured results, paths having the same impinging angle yet different delays exist due to the path bouncing in the LOS direction. The estimated PADP based on the virtual UCA with the proposed algorithm for the LOS scenario is shown in Fig. 10 (below), where in total 10 paths are detected. An excellent match of the measured PADPs between the rotational horn antenna and virtual UCA in terms of the number of propagation paths, azimuth angle, delay and power of each path can be observed. However, the measured results based on rotational horn antenna suffer from wide antenna beam-width, as expected. The proposed algorithm presents consistent parameter estimation, with high resolution in the angle and delay domains. Note that the antenna gains of the horn antenna and biconical antenna are calibrated out in the power spectra. Thus within the same power range, the same number of paths and approximately same path parameters can be observed in the plots. Furthermore, the estimated power of the LOS path (strongest path) is -76.5 dB, which matches well with the calculated path loss according to Friis equation with $D = 5$ m and $f_c = 29$ GHz, i.e. -75.7 dB. The deviation might be introduced by the inaccureate data in antenna gains and measurement uncertainties.

The measured CIRs and synthetic CIRs over virtual UCA elements for the OLOS scenario are shown in Fig. 11. A good agreement between the synthetic and measured CIRs can still be observed, though there exists many weak multipath components in the measured CIRs. The measured PADP with rotational horn antenna and virtual UCA with the proposed algorithm for the OLOS scenario are shown in Fig. 12, where 27 paths in total are detected within the dynamic range of 30 dB. Within the same power range, the channel parameters, e.g. the number of paths and path paramters, agree well between the rotational horn and the virtual UCA for the more critical OLOS scenario.

As observed in the measured CIRs over array elements, channel non-stationarity exists where different channel profiles can be observed by different array elements. This can be caused by several reasons, e.g. the power variation over the UCA elements in the near-field scenarios as explained; the coherent summation of unresolved multipath components due to limited system bandwidth; limited angle of view from the near-field scatterers and the measurement system non-idealities. The channel non-stationarity is not addressed in the proposed algorithm, as seen in the synthetic CIRs over UCA elements. Though channel non-stationarity has been considered in channel modeling works, e.g. [36], it has not been considered in the channel estimation in the literature so far due to high computation complexity.

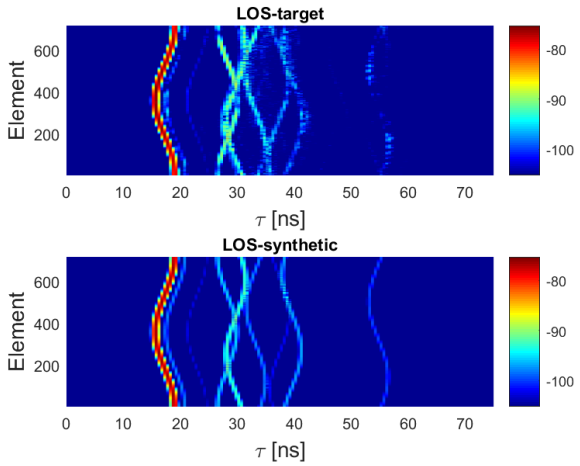

Figure 9. Measured CIRs (top) and synthetic CIRs (below) over virtual UCA elements for the LOS scenario.

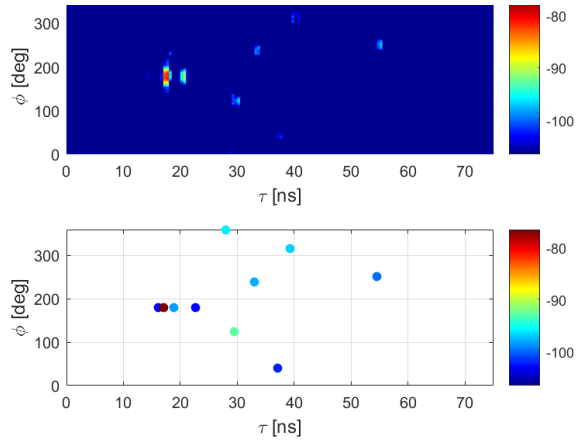

Figure 10. Measured PADPs with rotational horn antenna (top) and virtual UCA with the proposed algorithm (below) for the LOS scenario.

VI. CONCLUSION

Multipath parameter estimation for UWB large-scale UCA antenna systems is challenging, due to the fact that the well adopted plane-wave and narrowband assumptions might not hold. In this paper, a novel beamspace UCA algorithm based on phase mode excitation principle is proposed. The proposed beamformer can maintain approximately same beam patterns, independent of distance between the array and scatterer location, and of the system bandwidth, making it suitable for UWB near-field scenarios. The proposed algorithm has low computational cost since it avoids expensive joint estimation in multiple parameter domains. To remove the strong sidelobes of the proposed beamspace beamformer, a novel algorithm based on the successive cancellation principle is proposed for a given elevation angle range, i.e. $\Delta\theta = |\theta - 90^o| \leq 45^o$. Both numerical simulations and experimental measurements demonstrated the effectiveness and robustness of the proposed algorithm. The proposed algorithm is a general low-cost

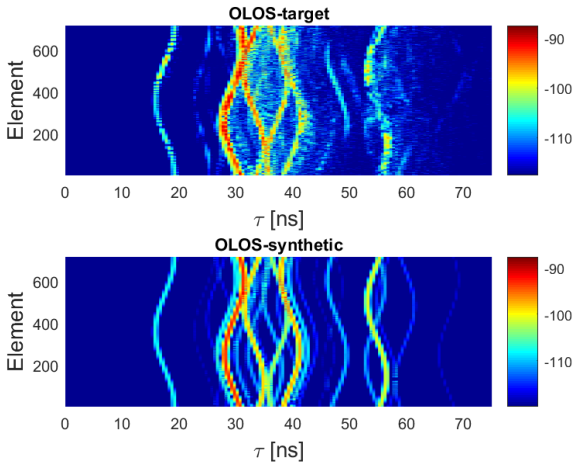

Figure 11. Measured CIRs (top) and synthetic CIRs (below) over virtual UCA elements for the OLOS scenario.

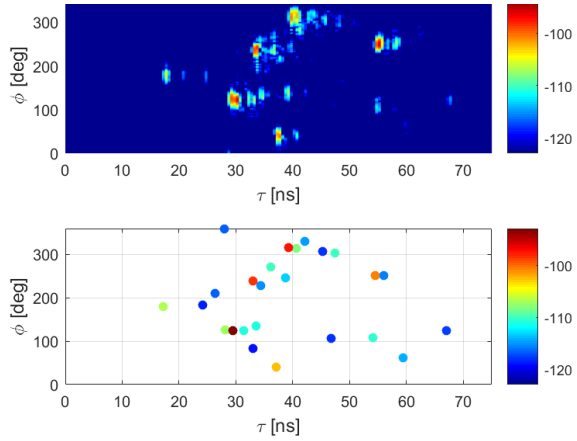

Figure 12. Measured PADPs with rotational horn antenna (top) and virtual UCA with the proposed algorithm (below) for the OLOS scenario.

channel estimator, since it works in near-field scenario for UWB system.

Further, due to the fact that the proposed beamformer pattern is not sensitive to the elevation angle and scatterer location, the proposed algorithm would fail to detect the elevation angle and scatter location. A high resolution propagation parameter estimation algorithm, which is capable of estimating all propagation parameters in the 3D near-field conditions is missing in the literature due to the fatal computation complexity. Our proposed algorithm, which offers high resolution azimuth angle, delay and complex amplitude estimation in a low-cost manner, can be utilized in the initial stage of the full parameter estimation algorithm, e.g. the MLE, which can significantly reduce the computation complexity due to the reduced searching space. This work will be carried out in the future.

REFERENCES

[1] T. S. Rappaport, S. Sun, R. Mayzus, H. Zhao, Y. Azar, K. Wang, G. N. Wong, J. K. Schulz, M. Samimi, and F. Gutierrez, "Millimeter wave mobile communications for 5g cellular: It will work!" *IEEE access*, vol. 1, pp. 335–349, 2013.

[2] J. G. Andrews, S. Buzzi, W. Choi, S. V. Hanly, A. Lozano, A. C. Soong, and J. C. Zhang, "What will 5g be?" *IEEE Journal on selected areas in communications*, vol. 32, no. 6, pp. 1065–1082, 2014.

[3] P. Demestichas, A. Georgakopoulos, D. Karvounas, K. Tsagkaris, V. Stavroulaki, J. Lu, C. Xiong, and J. Yao, "5g on the horizon: Key challenges for the radio-access network," *IEEE Vehicular Technology Magazine*, vol. 8, no. 3, pp. 47–53, 2013.

[4] R. He, B. Ai, G. L. Stüber, G. Wang, and Z. Zhong, "Geometrical-based modeling for millimeter-wave mimo mobile-to-mobile channels," *IEEE Transactions on Vehicular Technology*, vol. 67, no. 4, pp. 2848–2863, April 2018.

[5] R. He, B. Ai, G. L. Stüber, and Z. Zhong, "Mobility model based non-stationary mobile-to-mobile channel modeling," *IEEE Transactions on Wireless Communications*, pp. 1–1, 2018.

[6] K. Guan, G. Li, T. Kürner, A. F. Molisch, B. Peng, R. He, B. Hui, J. Kim, and Z. Zhong, "On millimeter wave and thz mobile radio channel for smart rail mobility," *IEEE Transactions on Vehicular Technology*, vol. 66, no. 7, pp. 5658–5674, July 2017.

[7] F. Rusek, D. Persson, B. K. Lau, E. G. Larsson, T. L. Marzetta, O. Edfors, and F. Tufvesson, "Scaling up mimo: Opportunities and challenges with very large arrays," *IEEE signal processing magazine*, vol. 30, no. 1, pp. 40–60, 2013.

[8] E. G. Larsson, O. Edfors, F. Tufvesson, and T. L. Marzetta, "Massive mimo for next generation wireless systems," *IEEE communications magazine*, vol. 52, no. 2, pp. 186–195, 2014.

[9] J. Medbo, K. Börner, K. Haneda, V. Hovinen, T. Imai, J. Järvelainen, T. Jämsä, A. Karttunen, K. Kusume, J. Kyröläinen *et al.*, "Channel modelling for the fifth generation mobile communications," in *The 8th European Conference on Antennas and Propagation (EuCAP 2014)*. IEEE, 2014, pp. 219–223.

[10] T. Jämsä, P. Kyösti, and K. Kusume, "Deliverable d1. 2 initial channel models based on measurements," *METIS project Deliverable*, 2014.

[11] P. Ferrand, M. Amara, S. Valentin, and M. Guillaud, "Trends and challenges in wireless channel modeling for evolving radio access," *IEEE Communications Magazine*, vol. 54, no. 7, pp. 93–99, 2016.

[12] C.-X. Wang, J. Bian, J. Sun, W. Zhang, and M. Zhang, "A survey of 5g channel measurements and models," *IEEE Communications Surveys & Tutorials*, vol. 20, no. 4, pp. 3142–3168, 2018.

[13] C. Gustafson, K. Haneda, S. Wyne, and F. Tufvesson, "On mm-wave multipath clustering and channel modeling," *IEEE Transactions on Antennas and Propagation*, vol. 62, no. 3, pp. 1445–1455, 2014.

[14] R. He, B. Ai, A. F. Molisch, G. L. Stuber, Q. Li, Z. Zhong, and J. Yu, "Clustering enabled wireless channel modeling using big data algorithms," *IEEE Communications Magazine*, vol. 56, no. 5, pp. 177–183, 2018.

[15] M. Dohler, F. Said, and H. Aghvami, "Concept of virtual antenna arrays," in *Proc. IEEE Globecom 2002*, 2002.

[16] J. Medbo, H. Asplund, and J.-E. Berg, "60 ghz channel directional characterization using extreme size virtual antenna array," in *Personal, Indoor, and Mobile Radio Communications (PIMRC), 2015 IEEE 26th Annual International Symposium on*. IEEE, 2015, pp. 176–180.

[17] A. W. Mbugua, W. Fan, Y. Ji, and G. F. Pedersen, "Millimeter wave multi-user performance evaluation based on measured channels with virtual antenna array channel sounder," *IEEE10:12 07-05-2018 Access*, 2018.

[18] B. Ai, K. Guan, R. He, J. Li, G. Li, D. He, Z. Zhong, and K. M. S. Huq, "On indoor millimeter wave massive mimo channels: Measurement and simulation," *IEEE Journal on Selected Areas in Communications*, vol. 35, no. 7, pp. 1678–1690, July 2017.

[19] D. Davies, "Circular arrays," *The handbook of antenna design*, vol. 2, pp. 299–329, 1983.

[20] I. Longstaff, P. Chow, and D. Davies, "Directional properties of circular arrays," in *Proceedings of the Institution of Electrical Engineers*, vol. 114, no. 6. IET, 1967, pp. 713–718.

[21] W. Fan, I. Carton, J. Ø. Nielsen, K. Olesen, and G. F. Pedersen, "Measured wideband characteristics of indoor channels at centimetric and millimetric bands," *EURASIP Journal on Wireless Communications and Networking*, vol. 2016, no. 1, p. 58, 2016.

[22] A. H. Tewfik and W. Hong, "On the application of uniform linear array bearing estimation techniques to uniform circular arrays," *IEEE Transactions on Signal Processing*, vol. 40, no. 4, pp. 1008–1011, 1992.

[23] C. Gentile, A. J. Braga, and A. Kik, "A comprehensive evaluation of joint range and angle estimation in indoor ultrawideband location systems," *EURASIP Journal on Wireless Communications and Networking*, vol. 2008, no. 1, p. 248509, 2008.

[24] S.-C. Chan and C. K. Pun, "On the design of digital broadband beamformer for uniform circular array with frequency invariant characteristics," in *Circuits and Systems, 2002. ISCAS 2002. IEEE International Symposium on*, vol. 1. IEEE, 2002, pp. I–I.

[25] M. D. Zoltowski and C. P. Mathews, "Direction finding with uniform circular arrays via phase mode excitation and beamspace root-music," in *Acoustics, Speech, and Signal Processing, 1992. ICASSP-92., 1992 IEEE International Conference on*, vol. 5. IEEE, 1992, pp. 245–248.

[26] M. D. Zoltowski, M. Haardt, and C. P. Mathews, "Closed-form 2-d angle estimation with rectangular arrays in element space or beamspace via unitary esprit," *IEEE Transactions on Signal Processing*, vol. 44, no. 2, pp. 316–328, 1996.

[27] M. Pesavento and J. Bohme, "Direction of arrival estimation in uniform circular arrays composed of directional elements," in *Sensor Array and Multichannel Signal Processing Workshop Proceedings, 2002*. IEEE, 2002, pp. 503–507.

[28] F. Belloni and V. Koivunen, "Unitary root-music technique for uniform circular array," in *Signal Processing and Information Technology, 2003. ISSPIT 2003. Proceedings of the 3rd IEEE International Symposium on*. IEEE, 2003, pp. 451–454.

[29] C. P. Mathews and M. D. Zoltowski, "Eigenstructure techniques for 2-d angle estimation with uniform circular arrays," *IEEE Transactions on signal processing*, vol. 42, no. 9, pp. 2395–2407, 1994.

[30] M. C. Vanderveen, C. B. Papadias, and A. Paulraj, "Joint angle and delay estimation (jade) for multipath signals arriving at an antenna array," *IEEE Communications letters*, vol. 1, no. 1, pp. 12–14, 1997.

[31] A.-J. Van Der Veen, M. C. Vanderveen, and A. J. Paulraj, "Joint angle and delay estimation using shift-invariance properties," *IEEE Signal Processing Letters*, vol. 4, no. 5, pp. 142–145, 1997.

[32] Y. Ji, W. Fan, and G. F. Pedersen, "Channel estimation using spherical-wave model for indoor los and obstructed los scenarios," in *Antennas and Propagation (EUCAP), 2017 11th European Conference on*. IEEE, 2017, pp. 2459–2462.

[33] ——, "Channel characterization for wideband large-scale antenna systems based on a low-complexity maximum likelihood estimator," *IEEE Transactions on Wireless Communications*, vol. 17, no. 9, pp. 6018–6028, 2018.

[34] B. H. Fleury, M. Tschudin, R. Heddergott, D. Dahlhaus, and K. I. Pedersen, "Channel parameter estimation in mobile radio environments using the sage algorithm," *IEEE Journal on selected areas in communications*, vol. 17, no. 3, pp. 434–450, 1999.

[35] F. Zhang, W. Fan, and G. F. Pedersen, "Frequency-invariant uniform circular array for wideband mm-wave channel characterization," *IEEE Antennas and Wireless Propagation Letters*, vol. 16, pp. 641–644, 2017.

[36] R. He, B. Ai, G. L. Stüber, and Z. Zhong, "Mobility model based non-stationary mobile-to-mobile channel modeling," *IEEE Transactions on Wireless Communications*, 2018.